Eur. Phys. J. B **51**, 137–143 (2006)
DOI: 10.1140/epjb/e2006-00197-6

THE EUROPEAN PHYSICAL JOURNAL B

Dry microfoams: formation and flow in a confined channel

J.-P. Raven[a], P. Marmottant, and F. Graner

Laboratoire de Spectrométrie Physique, CNRS - UMR 5588, Université Grenoble I, B.P. 87, 38402 St Martin d'Hères Cedex, France

Received 11 January 2006
Published online 31 May 2006 –

Abstract. We present an experimental investigation of the agglomeration of microbubbles into a 2D microfoam and its flow in a rectangular microchannel. Using a flow-focusing method, we produce the foam in situ on a microfluidic chip for a large range of liquid fractions, down to a few percent in liquid. We can monitor the transition from separated bubbles to the desired microfoam, in which bubbles are closely packed and separated by thin films. We find that bubble formation frequency is limited by the liquid flow rate, whatever the gas pressure. The formation frequency creates a modulation of the foam flow, rapidly damped along the channel. The average foam flow rate depends non-linearly on the applied gas pressure, displaying a threshold pressure due to capillarity. Strong discontinuities in the flow rate appear when the number of bubbles in the channel width changes, reflecting the discrete nature of the foam topology. We also produce an ultra flat foam, reducing the channel height from 250 μm to 8 μm, resulting in a height to diameter ratio of 0.02; we notice a marked change in bubble shape during the flow.

PACS. 47.60.+i Flows in ducts, channels, nozzles, and conduits – 83.50.Ha Flow in channels – 83.80.Iz Emulsions and foams

1 Introduction

Two phase microflows like the one of microemulsions, microbubbles, microdrops and recently ordered microbubble lattices attract considerable attention [1–5]. To these we would like to add a precise study of dry and controlled *microfoams*. Their application in a lab-on-a-chip context provides the possibility for the efficient handling of series of gas pockets, and allows to create microchemical reactors that are both very rapid and highly parallelized. Specifically, the gas-liquid interface of microfoams provides a transport location for amphiphilic molecules, with a hydrophilic head and a hydrophobic tail. A decrease in size increases the surface to volume ratio; hence, microfoams could be used as an efficient carrier for proteins or lipids at high concentration.

Microfoams offer advantages compared to foams at larger scales for the study of foam properties as microfoams are very stable and well controlled. First, the absence of vertical drainage on the small length scales of a microfluidic system creates liquid profiles in the foam films that are constant over time and do not show an asymmetry due to gravity. Another advantage is that because of the low Reynolds numbers involved, the amount of gas produced during bubbling is very stable with a nearly monodisperse bubble volume distribution. The amount of liquid (liquid fraction) can be reproducibly controlled as it is governed by the input parameters.

A set of basic operations using specific channel geometries necessary for manipulating series of bubbles, termed "discrete microfluidics", has been demonstrated at the millimeter scale [5] in a "dry" foam, where the liquid content is low compared to the gas content. To downscale these operations and adapt them for microfluidics requires producing a microfoam and information about its flow characteristics.

Here, we investigate the continuous production of a two phase gas-liquid flow in a flow-focusing device, and the transitions between different regimes of bubble formation, so as to reach microfoams, thereby extending the studies of reference [3] to low liquid fractions. In a microfluidic flow-focusing device, a flowing gas thread is forced, by the co-flowing surrounding liquid, into a small orifice, where the gas thread breaks up at regular time intervals [3,4,6]. At low liquid to total flow rate ratio this will create a microfoam.

We would like to determine how foam properties (for a review, see [7]) extrapolate to the micrometer range. We investigate here microfoam formation and flow dissipation within a microfluidic set-up: a bubble formation orifice, followed by a long channel ending with a free exit. We finally open perspectives for the study of structure and dissipation of ultra-flat microfoams.

[a] e-mail: jpraven@spectro.ujf-grenoble.fr

2 Materials and methods

We use a flow-focusing geometry: an inlet channel for the liquid, another one for the gas, both ending in an orifice ending up in a straight channel [1,3,4,6]. We produce the microfluidic device by soft lithography techniques. We first create a mold in a negative photosensitive material (SU-8 2100, MicroChem) and then make imprints in a polymer (polydimethylsiloxane, PDMS, Sylgard 184) to create the actual channel. The PDMS imprint is glued to a glass cover slide using a home-built ozone cleaner. The exit channel has a height $h = 250$ μm, width $w = 700$ μm and an orifice width $w_{or} = 100$ μm. We also use a channel where, at a distance of 6 mm after the orifice, the foam flows through a second constriction diminishing the channel width to 125 μm. We produce the ultra-flat foam in a device with a height of about $h = 8$ μm, width $w = 400$ μm and an orifice width $w_{or} = 75$ μm; we create the mold with a positive photo-resist (ma-P 100, Micro Resist Technology).

For the continuous phase we use deionized water with 10% commercial dishwashing detergent (Dreft, Procter & Gamble). This solution has a surface tension $\sigma = 38 \pm 1$ mN/m , as measured by the Wilhelmy balance method. The use of this surfactant resulted in an increased wettability of the solution to the PDMS surfaces [8]. Two different syringe pumps were used to push the liquid (11 Pico Plus, Harvard Apparatus, and KDS 100, KD Scientific) at flow rates Q_l ranging from 4 to 167 μl/min, with $\pm 0.5\%$ accuracy. The dispersed gas phase is nitrogen. It is driven at constant overpressure P_g (relative to one atmosphere), ranging from 1 to 21 kPa, using a pressurized tank and a pressure-reduction valve (stability ± 0.15 kPa). Pressure P_{in} is measured at the entrance of the device with a piezoresistive gauge (40PC Honeywell, ± 0.2 kPa accuracy). Since the exit is at atmospheric pressure $P_{out} = 1$ atm, the overpressure P_g is total gas pressure drop $P_{in} - P_{out}$ over the microfluidic system (orifice and channel).

In a typical experiment we vary the gas pressure while keeping the liquid flow rate constant. In this way we scan the complete pressure range for which bubbles are formed at that liquid flow rate. Still images or movies of the resulting flow are then captured with a camera (Marlin F131B, Allied Vision Technologies) connected to an inverted optical microscope (IX70, Olympus), see Figure 1b for some examples. By analysing these we can extract the following bubble quantities: formation rate (break-up frequency f), with a precision of a few percent, the bubble volume $V_b = A_b h$ by measuring the apparent area A_b occupied by the gas in the images, the gas flow rate estimated as $Q_g = V_b f$; and the space and time averaged gas velocity $\langle \overline{u_g} \rangle$ estimated as the distance between two consecutive bubbles multiplied by f. The edge of the measured area A_b (measured with a precision $\pm 1\%$) is taken in the middle of the curved meniscus around the bubble, appearing black on images. This introduces a systematic error in the measurement of the actual gas volume with an upper bound of 10% for small non-touching bubbles. In all cases the error is smaller than the symbol size used in Figure 1a.

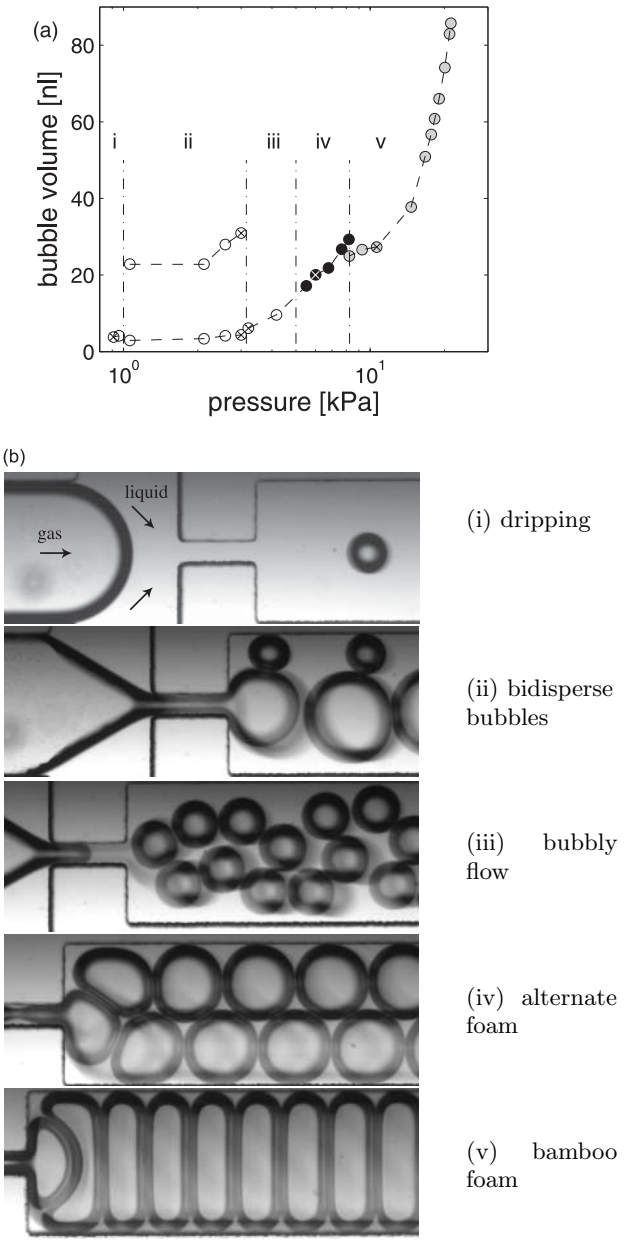

Fig. 1. From wet to dry microfoams. (a) Bubble volume V_b versus gas pressure P_g. Liquid flow rate is kept constant at $Q_l = 167$ μl min^{-1}. Numbers identify the different regimes: (i) dripping flow; (ii) bidisperse bubbles (two symbols are plotted for each pressure); (iii) bubbly flow; (iv) alternate foam (2 rows) with filled symbols; (v) bamboo foam (1 row) with gray symbols. (b) Photographs of these regimes. Crossed symbols in (a) correspond to pictures in (b).

An important parameter in characterizing a foam is the foam volume liquid fraction Φ_l, i.e. the proportion of the volume occupied by the liquid:

$$\Phi_l = \frac{V_l}{V_g + V_l}. \quad (1)$$

It is estimated by image analysis with $\Phi_l \simeq 1 - A_b/A$. Another method is to measure simultaneously the time

and space averaged bubble velocity $\langle\overline{u_g}\rangle$ together with the average gas flow rate; the liquid fraction then follows from $Q_g = \langle\overline{u_g}\rangle S(1-\Phi_l)$, with S the area of the channel cross section.

On the other hand, the proportion of liquid *injected* in the system is

$$\alpha_l = \frac{Q_l}{Q_g + Q_l}, \tag{2}$$

with $Q = Q_g + Q_l$ the total two-phase flow. It is simply measured as Q_l is one of the control parameters. The precision in this measurement is at minimum $\pm 10\%$ for non-touching bubbles and in general a few percent. The two quantities Φ_l and α_l are different because liquid and gas can have different velocities. They can be linked using the time and space averaged gas and liquid velocities $\langle\overline{u_g}\rangle$ and $\langle\overline{u_l}\rangle$ since $Q_l = \langle\overline{u_l}\rangle S\Phi_l$ and $Q_g = \langle\overline{u_g}\rangle S(1-\Phi_l)$. This yields:

$$\frac{\langle\overline{u_l}\rangle}{\langle\overline{u_g}\rangle} = \frac{\alpha_l}{1-\alpha_l}\frac{1-\Phi_l}{\Phi_l}. \tag{3}$$

The separate measurement of α_l and ϕ_l allows to calculate the ratio $\langle\overline{u_l}\rangle/\langle\overline{u_g}\rangle$ which informs about the relative drainage of liquid through the moving foam. The absence of relative drainage, $\langle\overline{u_l}\rangle/\langle\overline{u_g}\rangle = 1$, implies that $\alpha_l = \Phi_l$, while drainage in the direction of the flow, $\langle\overline{u_l}\rangle/\langle\overline{u_g}\rangle > 1$, entrains an injected liquid fraction higher than the volume liquid fraction $\alpha_l > \Phi_l$.

3 Microfoam formation at low liquid content

3.1 Bubbling regimes

To study bubble formation and the accompanying bubble topology in the channel we vary the gas pressure at constant liquid flow rate. See Figure 1 for examples of the observations in the 250 μm high channel, near the orifice at the channel entrance for a fixed flow rate of $Q_l = 167$ μl/min. Above a certain threshold in gas pressure P_g bubbles form in the channel. The bubble volume grows when increasing P_g, inducing several regimes of bubble formation and flow.

We observe a minimum pressure P_c for which bubbles form. For lower pressures the gas-liquid interface does not enter the orifice. At this liquid flow rate $P_c = 0.9 \pm 0.15$ kPa (Fig. 1a). This effect is probably due to the capillary pressure. For a curved interface in the orifice considering the limit of bubble detachment, the Laplace pressure of a wetting interface is

$$P_\sigma = \sigma\left(\frac{1}{r_1} + \frac{1}{r_2}\right) = 1.1 \pm 0.2 \quad \text{kPa}, \tag{4}$$

where $r_1 = h/2$ and $r_2 = w_{or}/2$ are the principal radii of curvature, of the same order as P_c.

Above the initial pressure P_c, a gas thread is forced into the orifice and fills a bubble after the orifice. This thread pinches off and releases the bubble. After breakup, the gas-liquid interface retracts to its initial position, as reported in [4], returning completely into the upstream part (dripping flow (i), Fig. 1b). At higher P_g, there is a coexistence, probably indicating a first-order transition, with a second mechanism, where the interface remains in the orifice instead of retracting after bubble release. For given P_g and Q_l, both mechanisms give different volumes V_1, V_2. This results in a flow of period $T_1 + T_2$ [3], with bidisperse bubbles (ii, Fig. 1b).

Further increasing P_g, we only observe the second pinch-off mechanism, always resulting in a monodisperse foam. Three possible structures appear, according to the flow rate: bubbly flow (iii), alternate foam with two rows (iv), or bamboo foam with one row only (v). No multiple-period or chaotic bubbling is observed. This suggests the absence of inertial non-linearities during the retraction of the gas-liquid interface [6].

For much higher P_g the gas thread stops breaking up and a stratified liquid-gas flow is observed.

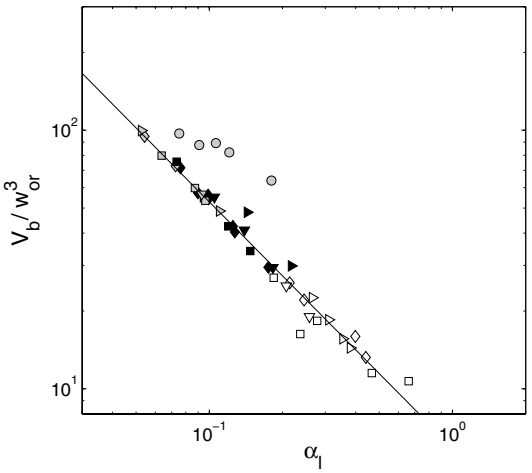

Fig. 2. The bubble volume V_b, in units of $w_{or}^3 = 1$ nl, depends only on the injected liquid fraction α_l. The solid line is a linear fit to all data except the lowest Q_l: $\log(V/w_{or}^3) = (-0.95 \pm 0.02)\log\alpha_l + (1.78 \pm 0.05)$. Symbols correspond to different values for the liquid flow rate $Q_l =$ (o) 4, ($\diamond$) 15, ($\square$) 20, ($\triangleright$) 30 and ($\triangledown$) 40 μl min^{-1}, for bubbly flows (open symbols), alternate foams (filled symbols), bamboo foams (gray symbols). For unknown reasons the data for $Q_l = 4$ μl min^{-1} diverges.

3.2 Microbubble volume

The bubble volume for the foam regimes (iii, iv and v) correlates well with the fluid fraction:

$$\frac{V_b}{w_{or}^3} \sim \alpha_l^{-0.95\pm0.02}, \tag{5}$$

see Figure 2, except for the lowest Q_l. At very low liquid content $\alpha_l \simeq Q_l/Q_g \ll 1$, bubble volumes are approximately proportional to $(Q_l/Q_g)^{-1}$.

This correlation is similar to the one observed in axisymmetric conditions by [9,10] who measured $V_b/w_{or}^3 \sim (Q_l/Q_g)^{-1.11\pm0.02}$, *in the opposite case* of high liquid fraction with $Q_l/Q_g > 5$, with separated bubbles,

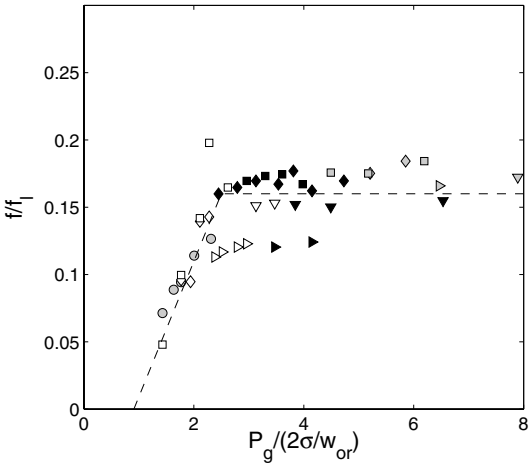

Fig. 3. The bubble formation frequency f in units of $f_l = Q_l/w_{or}^3$ vs. gas pressure P_g in units of $2\sigma/w_{or}$. It shows a plateau for high P_g: the dotted line is a piecewise linear fit. Symbols correspond to the same flow rates as in Figure 2.

while here bubbles are in contact or in short spacing after formation. It differs from the $V_b \sim P_g/Q_l$ scaling observed by Garstecki et al. [3]: we will see below that the gas flow rate and applied pressure are not proportional for a low liquid fraction microfoam in a channel. Moreover reference [3] investigates high liquid fraction flows at channel aspect ratio of 0.04 (flatter channels) much lower than the present 0.3. Both points could explain the experimentally observed differences.

In this geometry, one or two rows of bubbles are observed. The transition from bubbly flow to a foam in which bubbles touch each other is governed by the volume liquid fraction Φ_l, which is related to α_l through equation (3). Therefore increasing the number of bubble rows when the foam state appears would either require decreasing V_b at given Φ_l or enlarge the space for newly formed bubbles. The former can be achieved for instance with an orifice aspect ratio w_{or}/h closer to 1 to restrict liquid flow; and the latter by a lower ratio of orifice to channel width w_{or}/w.

3.3 Microbubble formation frequency

The frequency f of bubble formation (Fig. 3) first increases linearly then reaches a plateau for increasing P_g. The typical time and frequency linked to the liquid flow

$$\tau_l = \frac{1}{f_l} = \frac{w_{or}^3}{Q_l} \tag{6}$$

can be used to define a non-dimensional frequency, known as the Strouhal number,

$$St = \frac{f}{f_l} = \frac{f w_{or}^3}{Q_l}. \tag{7}$$

After rescaling by f_l all data collapse on a single curve where St is a function of gas pressure only. Two regimes are observed: for low gas pressures in the case of bubbly flow we find $St \simeq 0.1(P_g - P_c)/(2\sigma/w_{or})$, while for higher P_g, the Strouhal number saturates to a constant value of $St = 0.16$.

We infer that these two regimes are the consequence of two stages during the bubble formation:

1. Gas filling of the orifice: At low P_g the frequency varies like $f \sim f_l(P_g - P_c) \sim Q_l(P_g - P_c)$. In other words, the period is proportional to a characteristic time that varies as
$$T \simeq \tau_g \sim [Q_l(P_g - P_c)]^{-1}. \tag{8}$$
We interpret this time as the time necessary for the gas to fill the orifice, prior to break-up. It decreases with increasing $P_g - P_c$ since the gas pushes the fluid with a velocity increasing with pressure. τ_g also decreases for increasing Q_l with the flow-focusing confining more and more the available space for the gas thread. Note that the relation $f \sim Q_l P_g$ was proposed by [3], verified for varying Q_l but with a constant P_g or by keeping their product constant: here we also investigate the effect of gas pressure.
2. Liquid mediated thread pinch-off: For high P_g the bubble formation frequency is proportional to $f \sim Q_l$. The period only depends on
$$T \simeq \tau_l = \frac{w_{or}^3}{Q_l}, \tag{9}$$
the time to pinch off the gaseous thread when the liquid flow is blocked by the bubble at the outlet [4]. The physical meaning of w_{or}^3 is the volume initially occupied by the gas and then contracted by the liquid flow. This is in our case a part of the orifice but also a hard to quantify region upstream where the gas and liquid interface can also slightly move. The scaling in Figure 3 shows that w_{or} is an appropriate lengthscale to represent this volume.

The bubbling period at low pressure is limited by the gas filling, while it is limited by the liquid driven thread contraction in the high gas pressure regime. Note that the transition from a τ_g to a τ_l dominated break-up frequency is accompanied by the regime change from bubbly flow to foam. In the foam state, the liquid flow restriction seems more efficient (see Fig. 1b, iv and v).

As a conclusion, there are two stages during formation: the first associated with the filling of the orifice by the gas (τ_g) and the second reflecting the pinch-off of the gas thread (τ_l). They have different gas pressure dependency (τ_g depends on gas pressure while τ_l does not), which creates a cross-over apparent in the bubbling period $1/f$ that depends on τ_g and τ_l.

4 Foam flow

We now turn to the flow of a foam in the microchannel after formation. When we measure the average gas flow rate Q_g as a function of the applied gas pressure drop P_g, we observe a highly non-linear response (see Fig. 4). We

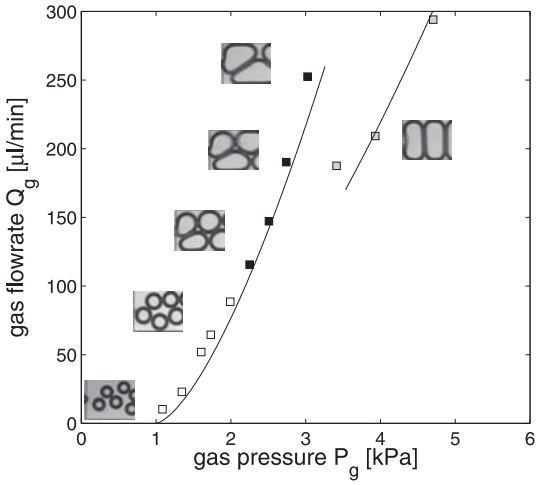

Fig. 4. Gas flow rate Q_g vs. gas pressure P_g showing a capillary threshold and discontinuity at the transition from alternate to bamboo foam ($Q_l = 20\ \mu\mathrm{l\,min^{-1}}$).

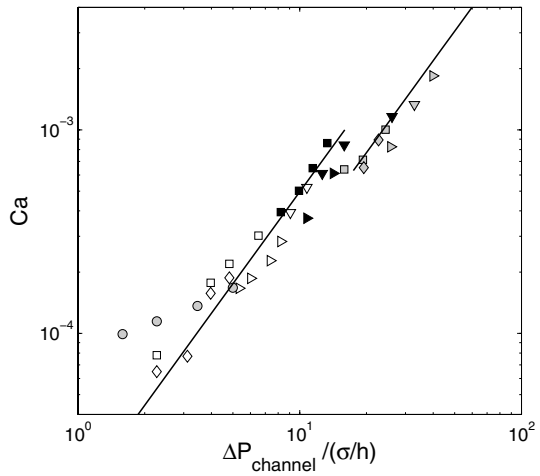

Fig. 5. Graph using adimensional axes $Ca = \mu Q_g/S\sigma$ versus $\Delta P_{channel} = P_g - P_c$. Data for different liquid flow rates are superimposed, $Q_l =$ (o) 4, (□) 20, (▷) 30 and (▽) 40 $\mu\mathrm{l\,min^{-1}}$. The solid lines on both plots are fit to data on alternate and bamboo foams at $Q_l = 20\ \mu\mathrm{l\ min^{-1}}$ with the power law $\Delta P_{channel}/(\sigma/h) = \beta\, Ca^{2/3}$, with $\beta = 1.7 \times 10^3$ (alternate) and $\beta = 2.5 \times 10^3$ (bamboo). For unknown reasons the data for $Q_l = 4\ \mu\mathrm{l\,min^{-1}}$ diverges.

find: a threshold (Sect. 4.1), a non-linear slope (Sect. 4.2) and a discontinuity upon the transition from an alternate to a bamboo foam (Sect. 4.3). The pulsation of the flow rate at the bubble formation frequency is finally examined (Sect. 4.4).

4.1 Pressure threshold

Figure 4 shows a threshold in pressure for the establishment of bubbly flow. It is found to be 1.0 ± 0.1 kPa, if this parameter is left free in the fit for liquid flow rates varying between 4 to 40 μl/min. It is compatible with the above explanation by a capillary effect (1.1 ± 0.2 kPa according to Eq. (4)) at the orifice and is within error boundaries equal to the value found for $Q_l = 167\ \mu$l/min.

In presence of a second constriction (data not shown), we obtain for regimes (iii) and (iv) the same result as in Figure 5, translated by about 0.45 kPa along the P-axis (compatible with the expected Laplace pressure necessary to overcome the second constriction, 0.6 kPa). This confirms that the threshold is induced by capillary effects. On the other hand, the slope originates from dissipative effects in the channel. We thus write the total pressure drop as the sum of two contributions,

$$P_g = P_c + \Delta P_{channel}, \tag{10}$$

where P_c is the static orifice contribution and $\Delta P_{channel}$ is due to dynamic dissipation in the channel.

4.2 Non-linear flow rate to pressure dependence

The flow rate is highly non-linear above the threshold, see Figure 4. The gas flow rate increases faster than a linear function of pressure for the alternate foam structure.

It can be interpreted by assuming that dissipation mainly occurs in the liquid films, close to the walls. Compared to a Newtonian flow whose drag pressure grows proportionally to the flow rate, the drag pressure grows with a lower exponent of the flow rate. It is an effect of the lubrication films between bubble and wall that thicken when flow rates increase, a phenomenon described first in [11], for the motion of a single bubble in a capillary tube establishing a relation of the form $\Delta P_{channel} \sim Ca^{2/3}$. The capillary number is defined as: $Ca = \mu v/\sigma$ (in our case of order $10^{-4} - 10^{-3}$) containing the bubble velocity v (estimated as $v \simeq Q_g/S$ in the dry foam state) and liquid viscosity μ. The prefactor in this relation relates to the friction due to the sliding of the films located between bubbles (connected to the wall by a Plateau border) over the wall [12] (see Fig. 8a). The pressure drop writes

$$\Delta P_{channel} = \overline{\lambda}\frac{nL_{proj}}{S}\sigma Ca^{2/3}, \tag{11}$$

with n the total number of bubbles in the channel, L_{proj} the projection on the cross section of the wetting perimeter per bubble (projected wall plateau border length), S the cross-section area, and $\overline{\lambda}$ a numerical constant [12]. The effect of the orientation of the films between bubbles relative to the foam movement is included in the L_{proj} variable ($L_{proj} = L\cos\alpha$ for a film whose normal vector is slanted by an angle α with respect to the flow direction).

In each regime, a fit of the pressure drop $\Delta P_{channel}$ by $Ca^{2/3}$ gives a correct agreement, see Figure 5.

We measure the projected friction length L_{proj} as the projection of the length between vertices centers, for contacts with the walls parallel to the image plane, neglecting side walls. We deduce for the numerical constant the value $\overline{\lambda} = 22 \pm 5$. The liquid coflow, varying over a decade, does not influence much the gas pressure drop in our geometry and the value of this constant (see Fig. 5). We can compare the constant $\overline{\lambda}$ between our microchannel and the millimetric channels with a comparable aspect ratio (but

without liquid coflow) studied by [12], who found $\overline{\lambda} = 38 \pm 4$. We observe less friction: in the present experiments liquid is injected continuously, possibly explaining wetter foams and a lower value for $\overline{\lambda}$. Since we see no visible change in the thickness of lubricating liquid films between gas and walls, which would change drag forces, we assume that liquid flows mostly in the corners [13]. Thanks to these corners in the square channel, that cannot be filled by a cylindrical bubble, the liquid flow is not as obstructed by bubbles in the channel as with a cylindrical geometry [11] (see Fig. 8b).

We find that the measured foam liquid fraction is close to the injected fraction $\Phi_l \simeq \alpha_l$: the liquid fraction is here controlled by the injection parameters. Using (3) we obtain $\langle \overline{u_l} \rangle / \langle \overline{u_g} \rangle \simeq 1$: there is no substantial relative drainage of the liquid within these foams. From conservation of liquid mass in the corners, we deduce that an increase of the liquid flow rate with no variation in average velocity should lead to an increase of the diameter of the corner.

4.3 Discontinuities in the flow-rate

The structure transition from an alternate to a bamboo foam induces a discontinuous decrease of the gas flow rate (Fig. 4).

This is a signature of the discrete character of the foam: we find by image analysis that the transition to bamboo structure is associated with an increase in the bubble number n of 15% (compactification). It is also associated with an increase of the projected length L_{proj} of 50%. Both factors are consistent with the observed increase of $\Delta P_{channel}$ by 50%, considering equation (11) that states that $\Delta P_{channel}$ is proportional to nL_{proj}. We conclude that the rearrangement of bubbles induces the discontinuity in the pressure drop.

A consequence of this finding is that, in some ranges, a given flow rate (here for Q_g in between 170 and 260 μl min^{-1}) can lead to two possible foam states, each one associated with a different pressure drop. This is of interest especially for gas flow rate instead of gas pressure controlled system in which it can lead to the intermittent existence of foam states.

4.4 Flow pulsation at bubbling frequency

The above flow rate measurements are in fact time-averaged flows. The foam velocity at the entrance oscillates at frequency f (Fig. 6a), between 3.1 and 8.3 cm/s. However, this oscillation is damped over a few mm along the channel (data not shown). Very little oscillation is observed at the channel exit (Fig. 6b).

Due to the periodic creation of bubbles, the pressure in the entrance orifice probably varies at frequency f. Each new bubble has to push the foam to create a place for itself; thus inducing the flow oscillation. Friction, probably mainly at the channel walls, homogenizes the flow at the micrometer scale. The forcing frequency is therefore gradually attenuated, allowing to consider the flow as steady

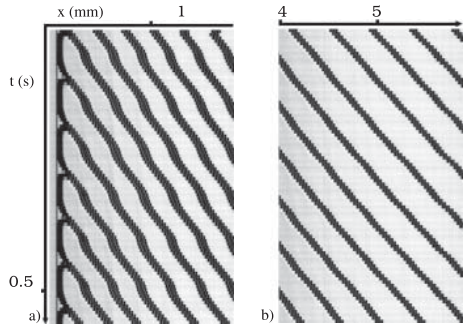

Fig. 6. Space-time diagrams of the foam flow in the constriction sample: (a) at the channel entrance; and (b) just before the exit constriction. The vertical axis is the time, flowing downwards; the horizontal axis is a (small zone of) the axis of the channel, with the foam flowing from left to right, $Q_l = 16.7$ μl min^{-1} and $P = 4.9$ kPa. Dark pixels indicate a bubble edge.

further in the channel, as if pushed by a steady pressure. In view of the use of foams in channels with obstacles, this would prevent resonance effects with the frequency of passage of bubbles on the obstacles downstream.

5 Ultraflat foam: distortion effects

In order to downscale flowing foams even more, we reduced the channel height to produce ultra-flat foams. The ultra-flat channel presents a 30-fold decrease in height, to 8 μm, and a 18-fold decrease in aspect ratio for the channel section, to 0.02. We continuously produce various foams in such a channel (Fig. 7), including one with 3 bubble rows (Fig. 7a).

We can dry it, using the following batch method. We shut the liquid inlet and pull the syringe at the gas inlet. As long as the underpressure is smaller than the Laplace threshold (here 11 kPa), the bubbles are blocked by the orifice and only liquid flows out of the foam. This forced drainage yields hexagons with a standard deviation in the edge length of only 1.8% (Fig. 7b). Since the apparent wall thickness on images (10 μm) is comparable to the height, the bubble walls are probably very curved (when looking at their profile on a cross-section perpendicular to the image plane), and with no flat film between bubbles, contrary to the previous set-up. At the walls the films form a wall plateau border with a typical radius about one half of the wall thickness measured on the projected image. If the channel height is order of two times this radius the wall Plateau borders start touching thereby excluding the possibility of a flat interface (see Fig. 8c). Thus the actual liquid fraction Φ_l of the central bubble row is probably smaller than, but close to, the apparent one (fraction of black pixels) $\Phi \approx \Phi_l^{image} \simeq 10^{-1}$. This contrasts with usual foams with larger aspect ratio, where the same picture of hexagons with straight walls and small vertices would correspond to much lower liquid fractions, $\Phi_l \simeq 10^{-2} < \Phi_l^{image}$ [7].

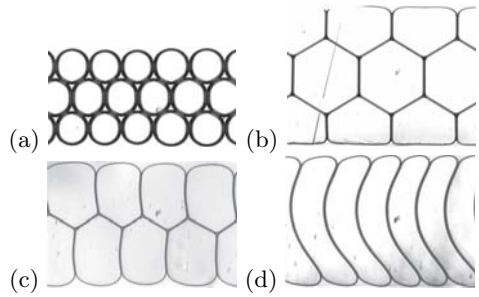

Fig. 7. Ultraflat foams in the 8 μm high channel: (a) flowing, wet and (b) static, dry 3-rows foams; (c) 2-rows and (d) 1-row flowing dry boomerang foams. Flows from left to right.

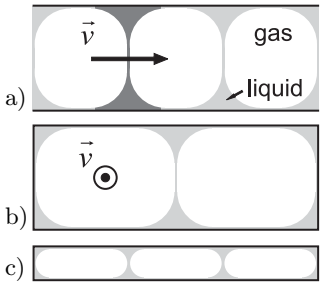

Fig. 8. Microchannel sections: (a) along the flow direction (arrow). Friction in the microchannel is mostly induced by the sliding of the film between bubbles over the wall. One of these films is indicated in dark grey. (b) perpendicularly to the motion. Water preferentially flows in the corners between bubble and wall and between bubbles. (c) perpendicularly to the motion, flat channel. The straight wall part in film between bubbles is absent due to the small aspect ratio. Note that the aspect ratio of the ultraflat channel used in the experiment is even a factor 5 smaller.

Foams flowing in this ultraflat channel undergo an unusual boomerang-like distortion, with films near the side walls pointing backwards (Figs. 7c,d), the opposite of foams with no coflowing liquid [5]. We indeed expect a larger friction at the center than on the edges, where bubble walls along the top and bottom plates are thin, than on the channel sides, where water accumulates. These edges are likely more entrained by a faster liquid flow than the centers ($\langle\overline{u_l}\rangle/\langle\overline{u_g}\rangle > 1$, assuming that for small aspect ratios corner sections are less expandable). Within the reference frame moving at the liquid velocity, the bubbles move in the opposite direction, from right to left. The distortion of bubble shapes in this reference frame, with films near the walls pointing forward, is then similar to the observations of millimetric bubbles pushed without any liquid flow [5].

6 Conclusions

We describe the formation and flow of a foam in a confined microchannel. The transition from bubbly flow to foam depends on Φ_l which is governed by the interplay between control parameters P_g and Q_l and the channel geometry. The frequency at which bubbles are formed behaves differently for bubbly flows and for foams. For foams the formation frequency only depends on the liquid flow rate controlling the speed at which the gas thread is pinched off. Foam flow and bubbly flow in microchannels are highly non-linear. The flow-focusing orifice induces a threshold P_c due to capillary effects in the flow rate to pressure characteristic. The data for both bubbly and foam flow give good agreement to $P_g - P_c \sim Ca^{2/3}$. The prefactor in this relation depends on the dissipation in the channel related to the topology.

Microfoams can be down-scaled to as small heights as 8 μm. The liquid fraction can be varied continuously over the complete range from the dry to the wet limit. We see an unusual deformation for foams flowing in this channel probably caused by relative drainage.

The interplay between geometrical parameters (channel aspect ratio, orifice aspect ratio and orifice to channel ratio) and the gas and liquid flow merits more attention. It governs various effects as the transition from bubbly flow to foam, the foam topology, and thereby dissipation in the channel, and the distortion of the foam cells. Comprehending this interplay will be a necessary step in the development of microfluidic applications in which the straight channel section will be replaced by more complex geometries allowing operations like mixing, separation, breaking and coalescence of bubbles.

We would like to thank W. Drenckhan for stimulating discussions, and T. Podgorski for his help on microchannel production.

References

1. S.L. Anna, N. Bontoux, H.A. Stone, Appl. Phys. Lett. **82**, 364 (2004)
2. T. Cubaud, C.M. Ho, Phys. Fluids **16**, 4575 (2004)
3. P. Garstecki, I. Gitlin, W. DiLuzio, G.M. Whitesides, Appl. Phys. Lett. **85**, 2649 (2004)
4. P. Garstecki, H. Stone, G. Whitesides, Phys. Rev. Lett. **94**, 164501 (2005)
5. W. Drenckhan, S. Cox, G. Delaney, D.W.H. Holste, N. Kern, Colloids and Surfaces A: Physicochem. Eng. Aspects **263**, 52 (2005)
6. P. Garstecki, M.J. Fuerstman, G.M. Whitesides, Phys. Rev. Lett. **94**, 234502 (2005)
7. D. Weaire, S. Hutzler, *The physics of foams* (Oxford University Press, 1999)
8. Y.H. Dou, N. Bao, J.J. Xu, H.Y. Chen, Electrophoresis **23**, 35583566 (2002)
9. A. Ganan-Calvo, J. Gordillo, Phys. Rev. Lett. **87**, 274501 (2001)
10. A. Ganan-Calvo, Phys. Rev. E **69**, 027301 (2004)
11. F.P. Bretherton, J. Fluid. Mech. **10**, 166 (1961)
12. I. Cantat, N. Kern, R. Delannay, Europhys. Lett. **65**, 726 (2004)
13. H. Wong, C.J. Radke, S. Morris, J. Fluid. Mech. **292**, 71 (1995)